Efficient mode exchanger-based silicon photonic switch enabled by inverse design

Zhang, Guowu; Xu, Dan-Xia; Grinberg, Yuri; Liboiron-Ladouceur, Odile

Publisher's version / Version de l'éditeur:
https://doi.org/10.1364/OE.456869
Optics Express, 30, 12, pp. 20543-20553, 2022-05-24

Research Article | Vol. 30, No. 12 / 6 Jun 2022 / Optics Express 20543
Optics EXPRESS

Efficient mode exchanger-based silicon photonic switch enabled by inverse design

GUOWU ZHANG,[1,*] DAN-XIA XU,[2] YURI GRINBERG,[2] AND ODILE LIBOIRON-LADOUCEUR[1]

[1]Department of Electrical and Computer Engineering, McGill University, Montréal, Quebec, H3A 0E9, Canada
[2]National Research Council Canada, Ottawa, ON K1A 0R6, Canada
[*]guowu.zhang@mail.mcgill.ca

Abstract: A novel and energy efficient mode insensitive switch building block is proposed and experimentally demonstrated on a silicon-on-insulator platform. Based on a Mach-Zehnder interferometer, the switch uses a relatively compact mode insensitive phase shifter which includes a mode exchanger. The novel structure realizes the exact same phase shift for all modes by exchanging the modes midway within the phase shifter. The design approach leads to reduced power consumption otherwise not possible. Switching the first two quasi transverse electric (TE) modes simultaneously consumes 25.6 mW of power, an approximately 30% reduction from previous reported demonstrations. The measured insertion loss is 3.1 dB on average with a worst-case crosstalk of −14.9 dB over a 40 nm optical bandwidth from 1530 nm to 1570 nm. The design methodology enables scalability up to four optical modes.

1. Introduction

Over the past few years, mode division multiplexing (MDM) has been investigated intensively to further increase the capacity of optical interconnect links in data centers. Compared with its counterparts, wavelength division multiplexing (WDM) and polarization division multiplexing (PDM), MDM employs orthogonal optical mode channels to transmit data, which only needs one light source and thus reduces the power consumption of the optical link [1]. Silicon-on-insulator (SOI) is an ideal technology platform for realizing MDM systems due to the large refractive index contrast between the silicon waveguide and the surrounding dioxide cladding. The compatibility of SOI with complementary metal-oxide-semiconductor (CMOS) also renders on-chip systems possible [2,3].

An MDM link is built from key building blocks such as mode multiplexers (MUXer) [4], multimode waveguide bends [5–7], multimode waveguide crossings [8], multimode 3 dB splitters [9], higher order mode filters [10], mode exchangers (ME) [11–15], multimode ring [16], multimode modulator [17], and multimode switches [18–26]. Among these, MDM multimode optical switches offer important operational functions as they add flexibility and reconfigurability to MDM-based systems.

According to their functionality, a multimode switch can be categorized as a space-based switch where all modes are switched onto a given output waveguide, and an intra-mode switch enabling reconfigurable data exchange between the various optical mode channels. In [20], a proposed general solution realizes multimode switching through a straightforward demultiplexing-switching-multiplexing method. In this method, the higher order modes are first demultiplexed onto a fundamental mode. Then, a conventional single-mode switch matrix realizes the desired switching configuration. At the switch output, the single mode channels are then multiplexed back onto the corresponding higher order modes. This solution inevitably increases the switch complexity and power consumption and degrades the insertion loss (IL) and crosstalk performance [20]. Aside from this approach, several other methods have been shown to realize multimode

#456869 https://doi.org/10.1364/OE.456869
Journal © 2022 Received 23 Feb 2022; revised 15 Apr 2022; accepted 13 May 2022; published 24 May 2022

Optics EXPRESS

switching. In [21,22], WDM-compatible MDM switches are proposed and demonstrated using microring resonators. Based on a densely packed waveguide array (DPWA), a two-mode switch is also demonstrated in [23]. Using symmetric Y-junctions and multimode interference (MMI) couplers, our group demonstrated a high-speed mode switch for switching between two modes using a PN junction-based phase shifter [24]. We also experimentally validated a four-port two mode MDM-based switch [25]. Cascaded MMI-based MDM mode switches were demonstrated in [26] using MMI as a mode decomposer leveraged by several single mode phase shifters. Recently, we demonstrated a mode insensitive switch for three TE modes using a balanced MZI structure with a mode insensitive phase shifter [27].

In this work, a novel, compact, and energy efficient mode insensitive switch designed for the first two TE modes is experimentally demonstrated. To eliminate the mode dependency of the phase shifter tuning efficiency, an inverse-designed and compact ME is inserted to maintain the exact same phase shift for all modes with low IL and crosstalk. Indeed, the ME in the middle of the phase shifter exchanges the input TE0 and TE1 modes ensuring that the total phase accumulation experienced by both modes is the same. The proposed structure differentiates itself from previous demonstrations [27,28] as it realizes an exact mode insensitive switching and enables a design with better tunning efficiency, leading to reduced power consumption. The switch consumes 25.6 mW when simultaneously switching the two TE modes using the thermal-optic effect, from 7.9 mW for the cross configuration to 33.5 mW for the bar configuration. The switching operation consumes less than 70% of the power consumption of previous MDM-based switch demonstrations [27]. This work shows an impactful application of inverse-designed photonic components where the same functionality with high efficiency would otherwise be difficult to realize using traditional components.

2. Design and characterization

The proposed device is designed for fabrication on an SOI chip with an optical waveguide thickness of 220 nm. The optical function is to perform a space-based switch on optical modes with improved efficiency. The input modes, TE0 and TE1, are simultaneously directed to either output port 1 or 2. The multimode waveguide width is 1.0 μm to support higher order modes. An on-chip adiabatic coupler-based mode multiplexer generates the TE1 mode [13]. The parameters of this mode (de)multiplexers are selected according to our previous work [27] and further optimized according to [13]. The structure of the mode multiplexer together with the optimized parameters are shown in Fig. 1(a). The multimode output of the multiplexer feeds into an MMI-based 3-dB multimode splitter sending the optical input modes into the two branches of the Mach-Zehnder interferometer (MZI) structure [27]. The MMI-based 3-dB splitter works on the principle of general interference. The width is set to be 10 μm and the length is initially set to be $3L_\pi/2$. Here, L_π is the beat length of the MMI and can be estimated analytically once the width of the MMI is fixed [27]. The MMI length is further optimized numerically to be 362 μm using Lumerical eigenmode expansion (EME) solver. The signals in the respective two arms pass through the specially designed mode insensitive phase shifter, then recombine through another 3-dB splitter to form a balanced MZI structure. At the two output ports of the switch, another ME exchanges back the optical signals onto their original mode channel. The schematic of the proposed mode insensitive switch is shown in Fig. 1(b).

The designed mode insensitive phase shifter includes two multimode waveguides, one preceding the ME and one after (Fig. 1(c)). The ME is designed using our in-house topological based inverse design method detailed in the Appendix [13]. The design is compact with a footprint of 4 μm × 4 μm contributing to a reduced footprint for the phase shifter. The transmission spectrum for the ME obtained through simulation using Lumerical FDTD is shown in Fig. 1(e), showing 0.3 dB IL and −29.5 dB crosstalk at 1550 nm. To illustrate how the proposed phase shifter based on the thermos-optic effect operates, the tuning efficiency is investigated through simulation

Optics EXPRESS

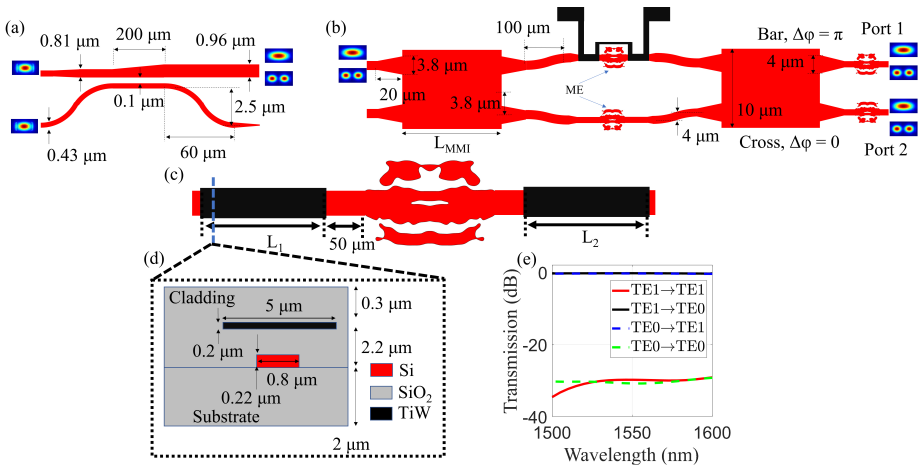

Fig. 1. (a) Schematic of the mode multiplexer and demultiplexer; (b) Schematic of the proposed mode insensitive switch; (c) Schematic of the proposed mode insensitive phase shifter; (d) Cross-section of the phase shifter; (e) Simulated transmission spectrum of the inverse designed ME.

as a function of the phase shifter waveguide width for the first four TE modes. The results shown in Fig. 2(a) indicate that for a waveguide width larger than 4 µm, the phase shifter enters an "approximately" mode insensitive region. This design region was previously used in our mode insensitive switch reported in [27]. One may notice in Fig. 2(a), however, that the tuning efficiency (dn_{eff}/dT) decreases as the phase shifter width increases which inevitably increases the power consumption of the switching operation. The optimum tuning efficiency for each optical mode occurs at a different waveguide width, forcing a compromise in the design. To solve this tradeoff between mode insensitivity and high-tuning efficiency, the proposed mode insensitive phase shifter shown in Fig. 2(d) consists of an input multimode waveguide of .. in length, the ME, followed by an output waveguide of L_2 in length. The optical phase of the TE0 mode (φ_{TE0}) and TE1 mode (φ_{TE1}) after this phase shifter can be expressed as the sum of the phase change from the input and output waveguides and the ME.

$$\varphi_{\mathrm{TE0}} = \frac{2\pi}{\lambda} \cdot n_{\,eff,\,\mathrm{TE0}} \cdot L_1 + \frac{2\pi}{\lambda} \cdot n_{\,eff,\,\mathrm{TE1}} \cdot L_2 + \varphi_{\mathrm{ME\_TE0\to TE1}} \tag{1}$$

$$\varphi_{\mathrm{TE1}} = \frac{2\pi}{\lambda} \cdot n_{\,eff,\,\mathrm{TE1}} \cdot L_1 + \frac{2\pi}{\lambda} \cdot n_{\,eff,\mathrm{TE0}} \cdot L_2 + \varphi_{\mathrm{ME\_TE1\to TE0}} \tag{2}$$

where $n_{\,eff,\ \mathrm{TE0}}$ and $n_{\,eff,\mathrm{TE1}}$ are the effective indices of the two modes respectively. Note that due to the symmetry of the ME along the Y-axis, the ME phase is the same for both modes ($\varphi_{ME\_TE0\to TE1} = \varphi_{ME\_TE1\to TE0}$). To characterize the temperature dependence of the proposed phase shifter, we define an equivalent tuning efficiency as the rate of phase change with respect to the temperature change ($d\varphi/dT$) per unit length divided by the wavenumber ($2\pi/\lambda$). To simplify the design and analysis, we assume that there is no phase change coming from the ME itself when the phase shifter is heated. In the chip layout, thus, the metal heater is placed 50 µm away from the ME to ensure this assumption is satisfied (shown in Fig. 1(c)). Accordingly, the corresponding equivalent tuning efficiency of the two modes can be expressed as the following,

$$\frac{\frac{d\varphi_{\mathrm{TE0}}}{dT}}{(L_1+L_2)\frac{2\pi}{\lambda}} = \frac{dn_{eff,\,\mathrm{TE0}}}{dT}\frac{L_1}{L_1+L_2} + \frac{dn_{eff,\,\mathrm{TE1}}}{dT}\frac{L_2}{L_1+L_2} \tag{3}$$

Optics EXPRESS

$$\frac{\frac{d\varphi_{\mathrm{TE1}}}{dT}}{(L_1+L_2)\frac{2\pi}{\lambda}} = \frac{dn_{eff,\,\mathrm{TE1}}}{dT}\frac{L_1}{L_1+L_2} + \frac{dn_{eff,\,\mathrm{TE0}}}{dT}\frac{L_2}{L_1+L_2} \tag{4}$$

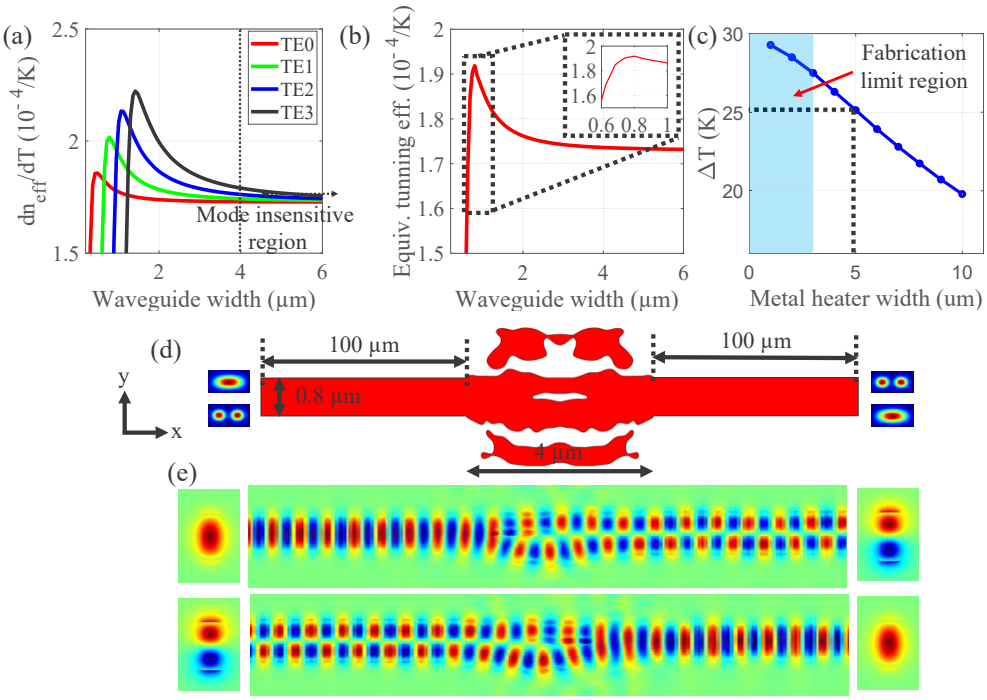

Fig. 2. (a) Simulated tuning efficiency as a function of the phase shifter width for the first four TE modes; (b) Simulated phase shifter "equivalent" tuning efficiency as a function of input and output multimode waveguide width for TE0 and TE1 input modes ($L_1 = L_2$) (Eq. (5) and (6)); (c) Simulated temperature increase as a function of metal heater width (black horizontal line describes temperature increase at the fabrication limit metal wire width); (d) Layout of the proposed mode insensitive phase shifter; (e) Simulated **Ey** component of the TE0 and TE1 propagating mode.

These equations provide a way to customize the tuning efficiency for TE0 and TE1 modes by varying L_1 and L_2. When both lengths are the same ($L_1 = L_2$), the equations simplify to the following,

$$\frac{\frac{d\varphi_{\mathrm{TE0}}}{dT}}{(L_1+L_2)\frac{2\pi}{\lambda}} = \frac{dn_{eff,\,\mathrm{TE0}}}{dT}\frac{1}{2} + \frac{dn_{eff,\,\mathrm{TE1}}}{dT}\frac{1}{2} \tag{5}$$

$$\frac{\frac{d\varphi_{\mathrm{TE1}}}{dT}}{(L_1+L_2)\frac{2\pi}{\lambda}} = \frac{dn_{eff,\,\mathrm{TE1}}}{dT}\frac{1}{2} + \frac{dn_{eff,\,\mathrm{TE0}}}{dT}\frac{1}{2} \tag{6}$$

The two equations become equivalent, independent of the width of the input and output multimode waveguides. Hence, a mode insensitive phase shifter can be realized for any waveguide width. The proposed structure, thus, gives the flexibility to change the phase shifter width to optimize the equivalent tuning efficiency (Fig. 2(b)). Through simulations, the multimode waveguide width is set to 0.8 μm to obtain the highest equivalent tuning efficiency possible. The corresponding simulated **Ey** component of the two propagating modes in the phase shifter is shown in Fig. 2(e). Note that both the tuning efficiency (Eqs. (5) and (6)) and the optical phase (Eqs. (1) and (2)) are the same at the output of the phase shifter. To further reduce the power consumption, the metal

Optics EXPRESS

heater width above the phase shifter is optimized using Lumerical Device. Figure 2(c) shows the simulated temperature increase for a 100 µm long and 0.8 µm wide waveguide phase shifter as a function of the metal width for a constant 20 mW power consumption. Narrower metal naturally leads to higher tuning efficiency since wider metal wire inefficiently diffuses heat to the waveguide below. On the other end, the fabrication process we used constrains the narrowest metal width possible to 3 µm. We select 5 µm for the metal width avoiding the fabrication limit while maintaining relatively high-tuning efficiency.

3. Experimental results

The device is fabricated using a 100 keV electron beam lithography (EBL) at Applied Nanotools (ANT) [29]. The silicon device layer patterning is followed by an inductively coupled plasma-induced reactive ion etching (ICP-RIE) process. A tungsten-titanium alloy (Ti/W) thin film as the metal heater and a thin aluminum film for metal routing are deposited using electron beam evaporation. A thin (300 nm) SiO_2 passivation layer is deposited by chemical vapor deposition (CVD) to protect the metal layers. The optical images for different parts of the fabricated switch are shown in Fig. 3(a) – (c). The SEM images for the fabricated MEs inside the phase shifter are shown in Fig. 3(d) and (e) to confirm the ME design is transferred onto the silicon layer.

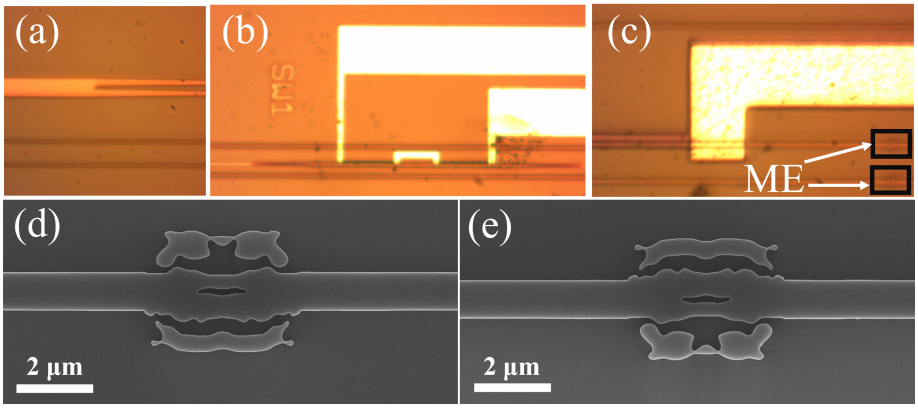

Fig. 3. The optical images for different parts of the fabricated switch: (a) MMI; (b) Phase shifter with metal heater; (c) ME; SEM images for the fabricated MEs of the (d) upper arm and (e) lower arm.

Continuous wave (CW) measurements are performed first using a Keysight C-band tunable laser. The output of the laser source is connected to a polarization controller (PC), then coupled onto the chip through an out-of-plane grating coupler. The output of the device is coupled out through another grating coupler. The optical output is measured using an ILX Lightwave optical power meter. All CW measurements are normalized to a loop back structure that connects two grating couplers through a short waveguide. The measured IL for the loop back structure is approximately 16 dB at 1550 nm.

Figure 4(a) and (b) show the normalized optical output power as a function of the applied electrical power to the phase shifter at 1550 nm for the TE0 and TE1 modes. Figure 4(c) is the measured I-V curve of the fabricated metal heater, indicating a resistance of 357 Ω. For TE0 mode, a power of 9.5 mW and 34.5 mW is needed to configure the switch in the cross and bar ports, respectively. The bar state configuration of the switch corresponds to when the top and bottom input ports connect to output ports 1 and 2, respectively (Fig. 1(b)). The cross state configuration connects the top input port to the bottom output port 2, and the bottom input to the top output port 1. The power for a π phase shift (Pπ) for TE0 mode is 25 mW. While for TE1

Optics EXPRESS

mode, 6.1 mW (32.8 mW) is needed to configure the switch in the cross (bar) port leading to Pπ = 26.7 mW. In Fig. 4(d), there is a 3.4 mW (1.7 mW or 6%) difference for TE0 and TE1 mode to realize a cross (bar) switching. These measurement results deviate slightly from the theoretical prediction where the Pπ is supposed to be the same. One likely reason for this residue difference is that L_1 and L_2 are only theoretically identical. In practice, there may be minor differences considering the imperfection fabrication process leading to a tuning efficiency difference between TE0 and TE1 modes. Simulations show that a 20 nm L1/L2 width deviation from the symmetric condition will cause a ~ 2% difference in Pπ. On the other hand, two separate heaters on top of these two parts would enable an exact mode insensitivity as different voltages can be applied to compensate the difference between L_1 and L_2 due to the fabrication. The cross (bar) state power is fixed at the crossing point of the measured transmission curves for TE0 and TE1 modes as 7.9 mW and 33.5 mW. This tradeoff causes minor degradation on the switching ON/OFF ratio (or extinction ratio, ER) performance as shown in Fig. 4(d). The corresponding extinction ratios are 19.5 dB (23.7 dB) and 18.3 dB (23.4 dB) for the "cross" ("bar") configuration for TE0 and TE1 mode, respectively.

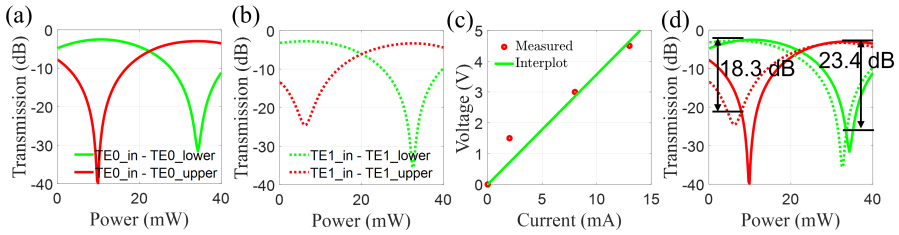

Fig. 4. Measured transmission at the upper and lower output waveguides as a function of applied electrical power to the phase shifter for (a) TE0 and (b) TE1 input at 1550 nm; (c) Measured and interpolated V-I curve for the fabricated metal heater; (d) Overlay of (a) and (b) to illustrate the difference in Pπ between TE0 and TE1 inputs of the phase shifter.

The transmission spectrum is then characterized for the fabricated MDM switch. The normalized measured spectrum of the fabricated switch circuit, including the mode multiplexer and demultiplexer, and the switch, for the TE0 and TE1 modes are shown in Fig. 5(a)-(d). Within the 40-nm optical bandwidth from 1530 nm to 1570 nm, the average IL for TE0 is 2.7 dB with values ranging from 3.5 dB to 2.0 dB, with the worst modal crosstalk at most −16 dB. Within the same optical bandwidth, for TE1 mode, the average IL is 3.1 dB ranging between 4.1 dB and 2.5 dB, with a worst modal crosstalk of −14 dB. Approximately half of the IL comes from the mode multiplexer and demultiplexer corresponding to approximately 1 dB and 1.3 dB at 1550 nm for the TE0 and TE1 respectively. For MMI, the IL is around 0.3 dB and 0.8 dB for TE0 and TE1 inputs at the same wavelength. One ME has around 0.35 dB IL at 1550 nm. The detailed performance of the MDM switch at 1550 nm is summarized in the Table 1.

Table 1. Experimental Results of the Switch at 1550 nm

Performance	Modes		
	TE0 Cross (Bar)	TE1 Cross/(Bar)	Difference Cross/(Bar)
IL (dB)	2.4 (2.3)	2.8(3.1)	0.4(0.8)
ER (dB)	19.5 (23.7)	18.3(23.4)	0.8(0.3)
XT (dB)	−16 (−15.5)	−14.9(−17.2)	1.1(1.7)
P_π (mW)	25 (25)	26.7(26.7)	1.7(1.7)
BW (nm)	40 (40)	40(40)	0(0)

Optics EXPRESS

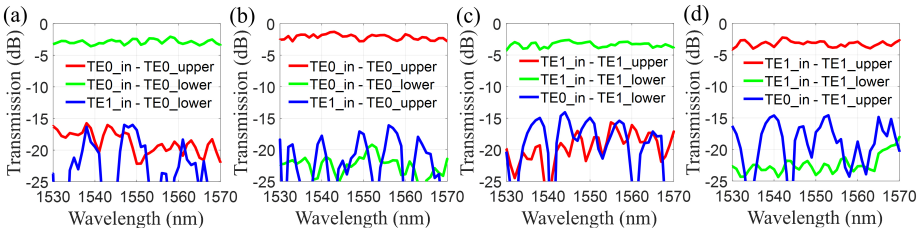

Fig. 5. Normalized measured transmission spectra of the MDM switch for (a) TE0 input "cross" configuration; (b) TE0 input "bar" configuration; (c) TE1 input "cross" configuration; (d) TE1 input "bar" configuration.

4. Scalability of the proposed phase shifter

The scalability of the proposed energy efficient mode insensitive switch for higher order modes is investigated. TE modes are investigated in this work as we already have developed the necessary building blocks for our system applications. It is worth noting that the same principle works for TM modes as well. Further, it can be extended to a polarization division multiplexing (PDM) or even a PDM-MDM hybrid optical switch with proper modification. As a proof of concept, we show an energy efficient mode insensitive phase shifter using our proposed method for four modes. The schematic is shown in Fig. 6 where three MEs are needed. Due to the symmetry requirement, ME1 and ME3 are identical which exchanges TE0 mode with TE1 mode as well as TE2 mode with TE3 mode. While the ME2 exchanges mode TE0 with TE2 mode and TE1 mode with TE3 mode.

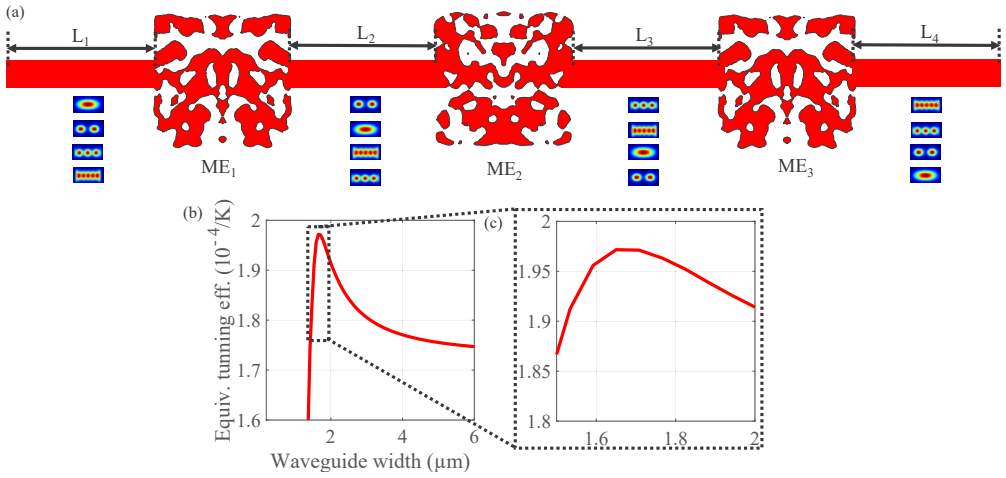

Fig. 6. (a) Schematic of the proposed energy efficient four-mode mode insensitive phase shifter. (b) Simulated phase shifter "equivalent" tuning efficiency as a function of input and output multimode waveguide width for TE0, TE1, TE2, and TE3 input modes. (c) Zoom in view of (b).

The optical phase for all the four modes is shown in Eq. (7–10). Note that the accumulated phase comes from the propagation of the modes and MEs as well. The accumulated optical phase for each mode from the MEs may be different. To make the accumulated phase from MEs the same, one may add phase transmission as a figure of merit (FOM) during the optimization for MEs [13]. With this configuration, the multimode waveguide lengths $L_1 = L_2 = L_3 = L_4$ are identical

Optics EXPRESS

leading to a tuning efficiency for all the four modes to be exactly the same under ideal conditions, realizing a mode insensitive phase shifter regardless of the multimode waveguide width. To investigate the improvement in power consumption, the simulated phase shifter "equivalent" tuning efficiency as a function of input and output multimode waveguide width for TE0, TE1, TE2, and TE3 input modes is presented in Fig. 6(b). To show the improvements of the power consumption, the Pπ of the conventional 6 μm wide mode insensitive and proposed phase shifter is calculated. The equivalent tuning efficiency for the conventional and proposed phase shifter are 1.73×10^{-4}/K and 1.98×10^{-4}/K, respectively. Note that the proposed phase shifter has the highest equivalent tuning efficiency at the waveguide width of 1.71 μm. From the simulation results, the equivalent tuning efficiency is improved by 15% of the conventional counterpart.

$$\varphi_{\mathrm{TE0}} = \tfrac{2\pi}{\lambda}\cdot n_{\mathrm{TE0}}\cdot L_1 + \tfrac{2\pi}{\lambda}\cdot n_{\mathrm{TE1}}\cdot L_2 + \tfrac{2\pi}{\lambda}\cdot n_{\mathrm{TE2}}\cdot L_3 + \tfrac{2\pi}{\lambda}\cdot n_{\mathrm{TE3}}\cdot L_4 + \varphi_{\mathrm{ME1\_TE0\to TE1}} + \varphi_{\mathrm{ME2\_TE1\to TE2}} + \varphi_{\mathrm{ME3\_TE2\to TE3}} \tag{7}$$

$$\varphi_{\mathrm{TE1}} = \tfrac{2\pi}{\lambda}\cdot n_{\mathrm{TE1}}\cdot L_1 + \tfrac{2\pi}{\lambda}\cdot n_{\mathrm{TE0}}\cdot L_2 + \tfrac{2\pi}{\lambda}\cdot n_{\mathrm{TE3}}\cdot L_3 + \tfrac{2\pi}{\lambda}\cdot n_{\mathrm{TE2}}\cdot L_4 + \varphi_{\mathrm{ME1\_TE1\to TE0}} + \varphi_{\mathrm{ME2\_TE0\to TE3}} + \varphi_{\mathrm{ME3\_TE3\to TE2}} \tag{8}$$

$$\varphi_{\mathrm{TE2}} = \tfrac{2\pi}{\lambda}\cdot n_{\mathrm{TE2}}\cdot L_1 + \tfrac{2\pi}{\lambda}\cdot n_{\mathrm{TE3}}\cdot L_2 + \tfrac{2\pi}{\lambda}\cdot n_{\mathrm{TE0}}\cdot L_3 + \tfrac{2\pi}{\lambda}\cdot n_{\mathrm{TE1}}\cdot L_4 + \varphi_{\mathrm{ME1\_TE2\to TE3}} + \varphi_{\mathrm{ME2\_TE3\to TE0}} + \varphi_{\mathrm{ME3\_TE0\to TE1}} \tag{9}$$

$$\varphi_{\mathrm{TE3}} = \tfrac{2\pi}{\lambda}\cdot n_{\mathrm{TE3}}\cdot L_1 + \tfrac{2\pi}{\lambda}\cdot n_{\mathrm{TE2}}\cdot L_2 + \tfrac{2\pi}{\lambda}\cdot n_{\mathrm{TE1}}\cdot L_3 + \tfrac{2\pi}{\lambda}\cdot n_{\mathrm{TE0}}\cdot L_4 + \varphi_{\mathrm{ME1\_TE3\to TE2}} + \varphi_{\mathrm{ME2\_TE2\to TE1}} + \varphi_{\mathrm{ME3\_TE1\to TE0}} \tag{10}$$

5. Conclusion

We design and experimentally demonstrate a novel energy efficient mode insensitive switch for MDM systems. The proposed phase shifter can realize exact mode insensitivity theoretically with 25.6 mW power consumption using thermo-optic tuning, approximately 30% less relative to previous demonstrations. The experimental results show that the switch exhibits 2.1 dB (2.7 dB) IL on average and less than −16 dB (−15.5 dB) crosstalk within the wavelength range of 40 nm (1530 nm – 1570 nm) for the cross (bar) states for TE0 modes. While for the TE1 mode, the IL is less than 2.8 dB (3.1 dB) on average and the crosstalk is less than −14.1 dB (−14.5 dB) within the same bandwidth. The measured switching extinction ratio for all the modes is better than 18 dB. The proposed switch structure is also scalable to even higher number of modes. We believe this work shows the potential application of inverse designed devices at a system level, highlighting the benefits beyond device area reduction. This paves the way for their more extensive use in a wide range of scenarios.

Appendix: inverse design of the mode exchanger

The optimization detail of the ME is given in this Appendix. In this work, topology optimization using the adjoint method is employed [30–43] to optimize an ME between the TE0 mode and the TE1 mode.

In our optimization configuration, the TE0 is excited at the input waveguide, with the goal of generating the TE1 mode at the output waveguide. The dimensions of the input and output waveguides, the design region, the symmetry axis (marked by the blue-dash line), and the position of the monitor (marked by the green-dash line) are shown in Fig. 7(a). Note that the permittivity of the ME is enforced to be symmetric along the Y-axis. The three-field (namely a design field, a filtered field, and a physical field) topology optimization scheme [42] is used to represent

Optics EXPRESS

permittivity distribution inside the design region. The mode overlap integral to the desired mode (TE1 mode), and the unwanted modes at the output waveguide are used to define the figure of merit (FOM) as,

$$FOM = \eta_{\mathrm{TE0}\rightarrow\mathrm{TE1}} - \tau\left(\eta_{\mathrm{TE0}\rightarrow\mathrm{TE0}} + \eta_{\mathrm{TE1}\rightarrow\mathrm{TE1}}\right) \tag{11}$$

where $\eta_{\mathrm{TEi}\rightarrow\mathrm{TEj}}$ represents the transmission of the input i-th TE mode into the j-thTE mode at the output waveguide, τ is a penalty weight that is used to balance the importance between transmission and crosstalk optimization. During the optimization, the algorithm tries to maximize the FOM. To achieve a broadband response, the optimization is carried out over five equally spaced wavelength points from 1500 nm to 1600 nm. The FOM as a function of the iteration is illustrated in Fig. 7(b).

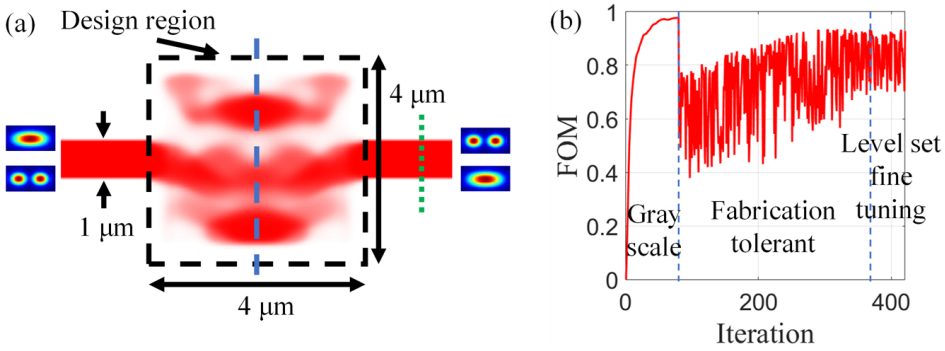

Fig. 7. (a) Illustration for the input/output relation of the ME (b) FOM as a function of iterations at 1550 nm.

The optimization is divided into three separated stages. In this first stage, namely gray scale optimization, all the permittivity inside the design domain is allowed to be between the permittivity of silicon dioxide and the permittivity of silicon. This corresponds to the first part of the curve in Fig. 7(b).

In the second stage, the design is further optimized to be robust towards fabrication imperfections. Random fabrication errors caused by over-etch and under-etch are considered in the design optimization which explains the fluctuation of the FOM in the second part of the curve in Fig. 7(b). Finally, a level-set method [39] is employed to fine-tune the boundary of the device from the previous step. Additionally, the crosstalk is added as a design objective during this step to further improve the performance of the ME device ($\tau = 5$ for the final stage, whereas $\tau = 0$ for the first two stages). The gradient of FOM is calculated using the adjoint method [30–43]. After the gradient is calculated, a gradient search-based algorithm, adaptive moment estimation (Adam), is employed to update the design variables.

Funding. National Research Council Canada (AI for Design and HTSN Challenge Programs); China Scholarship Council.

Disclosures. The authors declare that there are no conflicts of interest related to this article.

Data availability. Data underlying the results presented in this paper are not publicly available at this time but may be obtained from the authors upon reasonable request.

References

1. E. Agrell, M. Karlsson, A. R. Chraplyvy, D. J. Richardson, P. M. Krummrich, P. Winzer, K. Roberts, J. K. Fischer, S. J. Savory, B. J. Eggleton, and M. Secondini, "Roadmap of optical communications," J. Opt. **18**(6), 063002 (2016).
2. C. Li, D. Liu, and D. Dai, "Multimode silicon photonics," Nanophotonics **8**(2), 227–247 (2018).
3. Y. Xie, Y. Shi, L. Liu, J. Wang, R. Priti, G. Zhang, O. Liboiron-Ladouceur, and D. Dai, "Thermally-reconfigurable silicon photonic devices and circuits," IEEE J. Sel. Top. Quantum Electron. **26**(5), 1–20 (2020).

Optics EXPRESS

4. Y. Ding, J. Xu, F. Da Ros, B. Huang, H. Ou, and C. Peucheret, "On-chip two-mode division multiplexing using tapered directional coupler-based mode multiplexer and demultiplexer," Opt. Express **21**(8), 10376–10382 (2013).
5. H. Wu, C. Li, L. Song, H. K. Tsang, J. E. Bowers, and D. Dai, "Ultra-sharp multimode waveguide bends with subwavelength gratings," Laser Photonics Rev. **13**(2), 1800119 (2019).
6. X. Jiang, H. Wu, and D. Dai, "Low-loss and low-crosstalk multimode waveguide bend on silicon," Opt. Express **26**(13), 17680–17689 (2018).
7. H. Xu and Y. Shi, "Ultra-sharp multi-mode waveguide bending assisted with metamaterial-based mode converters," Laser Photonics Rev. **12**(3), 1700240 (2018).
8. H. Xu and Y. Shi, "Metamaterial-based maxwell's fisheye lens for multimode waveguide crossing," Laser Photonics Rev. **12**(10), 1800094 (2018).
9. W. Chang, X. Ren, Y. Ao, L. Lu, M. Cheng, L. Deng, D. Liu, and M. Zhang, "Inverse design and demonstration of an ultracompact broadband dual-mode 3 dB power splitter," Opt. Express **26**(18), 24135–24144 (2018).
10. X. Guan, Y. Ding, and L. H. Frandsen, "Ultra-compact broadband higher order-mode pass filter fabricated in a silicon waveguide for multimode photonics," Opt. Lett. **40**(16), 3893–3896 (2015).
11. C. Sun, Y. Yu, G. Chen, and X. Zhang, "Integrated switchable mode exchange for reconfigurable mode-multiplexing optical networks," Opt. Lett. **41**(14), 3257–3260 (2016).
12. M. Ye, Y. Yu, C. Sun, and X. Zhang, "On-chip data exchange for mode division multiplexed signals," Opt. Express **24**(1), 528–535 (2016).
13. G. Zhang and O. Liboiron-Ladouceur, "Scalable and Low Crosstalk Silicon Mode Exchanger for Mode Division Multiplexing System Enabled by Inverse Design," IEEE Photonics J. **13**(2), 1–13 (2021).
14. Y. Liang, Y. Xu, Y. Dong, B. Zhang, and Y. Ni, "Efficient silicon-based higher-order mode converters based on subwavelength grating slots," J. Opt. Soc. Am. B **38**(10), 2908–2914 (2021).
15. H. Jia, T. Zhou, X. Fu, J. Ding, and L. Yang, "Inverse-design and demonstration of ultracompact silicon meta-structure mode exchange device," ACS Photonics **5**(5), 1833–1838 (2018).
16. M. Ye, C. Sun, Y. Yu, Y. Ding, and X. Zhang, "Silicon integrated multi-mode ring resonator," Nanophotonics **10**(4), 1265–1272 (2021).
17. G. Zhou, Y. Guo, L. Lu, J. Chen, and L. Zhou, "Silicon reconfigurable mode-selective modulation for on-chip mode-multiplexed photonic systems," Opt. Lett. **46**(5), 1145–1148 (2021).
18. D. N. T. Hang, H. T. Duy, T. T. T. Thanh, N. D. H. Khoi, and C. D. Truong, "Compact, highly efficient, and controllable simultaneous 2× 2 three-mode silicon photonic switch in the continuum band," IEEE Access **9**, 102387–102396 (2021).
19. D. D. Quang, H. T. Duy, D. N. T. Hang, T. T. T. Thanh, T. A. Tran, L. H. D. Tam, T. H. Nguyen, B. D. Hoai, and C. D. Truong, "1× 3 reconfigurable and simultaneous three-mode selective router based on silicon waveguide utilizing Ti microheaters as thermo-optic phase shifters," Microelectronics J. **117**, 105278 (2021).
20. L. Yang, T. Zhou, H. Jia, S. Yang, J. Ding, X. Fu, and L. Zhang, "General architectures for on-chip optical space and mode switching," Optica **5**(2), 180–187 (2018).
21. H. Jia, S. Yang, T. Zhou, S. Shao, X. Fu, L. Zhang, and L. Yang, "WDM-compatible multimode optical switching system-on-chip," Nanophotonics **8**(5), 889–898 (2019).
22. B. Stern, X. Zhu, C. P. Chen, L. D. Tzuang, J. Cardenas, K. Bergman, and M. Lipson, "On-chip mode-division multiplexing switch," Optica **2**(6), 530–535 (2015).
23. K. Chen, J. Yan, S. He, and L. Liu, "Broadband optical switch for multiple spatial modes based on a silicon densely packed waveguide array," Opt. Lett. **44**(4), 907–910 (2019).
24. Y. Xiong, R. B. Priti, and O. Liboiron-Ladouceur, "High-speed two-mode switch for mode-division multiplexing optical networks," Optica **4**(9), 1098–1102 (2017).
25. A. Das, G. Zhang, H. R. Mojaver, and O. Liboiron-Ladouceur, "Scalable Two-Mode 3-Port and 4-Port Mode Insensitive Silicon Photonic Switches," IEEE Photonics Tech. Lett. **33**(11), 557–560 (2021).
26. R. B. Priti, G. Zhang, and O. Liboiron-Ladouceur, "3 × 10 Gb/s silicon three-mode switch with 120° hybrid based unbalanced Mach-Zehnder interferometer," Opt. Express **27**(10), 14199–14212 (2019).
27. G. Zhang, H. R. Mojaver, A. Das, and O. Liboiron-Ladouceur, "Mode insensitive switch for on-chip interconnect mode division multiplexing systems," Opt. Lett. **45**(4), 811–814 (2020).
28. C. Sun, Y. Ding, Z. Li, W. Qi, Y. Yu, and X. Zhang, "Key multimode silicon photonic devices inspired by geometrical optics," ACS Photonics **7**(8), 2037–2045 (2020).
29. Applied Nanotools Inc. Accessed: May 31, 2021. [Online]. Available: https://www.appliednt.com.
30. J. Lu and J. Vučković, "Nanophotonic computational design," Opt. Express **21**(11), 13351–13367 (2013).
31. J. Lu and J. Vučković, "Objective-first design of high-efficiency, small-footprint couplers between arbitrary nanophotonic waveguide modes," Opt. Express **20**(7), 7221–7236 (2012).
32. A. Y. Piggott, J. Lu, K. G. Lagoudakis, J. Petykiewicz, T. M. Babinec, and J. Vučković, "Inverse design and demonstration of a compact and broadband on-chip wavelength demultiplexer," Nat. Photon. **9**(6), 374–377 (2015).
33. S. Molesky, Z. Lin, A. Y. Piggott, W. Jin, J. Vucković, and A. W. Rodriguez, "Inverse design in nanophotonics," Nat. Photon. **12**(11), 659–670 (2018).
34. A. Y. Piggott, E. Y. Ma, L. Su, G. H. Ahn, N. V. Sapra, D. Vercruysse, and J. Vuckovic, "Inverse-designed photonics for semiconductor foundries," ACS Photonics **7**(3), 569–575 (2020).

Optics EXPRESS

35. M. P. Bendsoe and O. Sigmund, "*Topology optimization: theory, methods, and applications*," Springer Science & Business Media (2013).
36. N. Zhao, S. Boutami, and S. Fan, "Efficient method for accelerating line searches in adjoint optimization of photonic devices by combining Schur complement domain decomposition and Born series expansions," Opt. Express **30**(4), 6413–6424 (2022).
37. N. Zhao, S. Boutami, and S. Fan, "Accelerating adjoint variable method based photonic optimization with Schur complement domain decomposition," Opt. Express **27**(15), 20711–20719 (2019).
38. C. M. Lalau-Keraly, S. Bhargava, O. D. Miller, and E. Yablonovitch, "Adjoint shape optimization applied to electromagnetic design," Opt. Express **21**(18), 21693–21701 (2013).
39. A. Y. Piggott, J. Petykiewicz, L. Su, and J. Vučković, "Fabrication-constrained nanophotonic inverse design," Sci. Rep. **7**(1), 1786 (2017).
40. L. F. Frellsen, Y. Ding, O. Sigmund, and L. H. Frandsen, "Topology optimized mode multiplexing in silicon-on-insulator photonic wire waveguides," Opt. Express **24**(15), 16866–16873 (2016).
41. Y. Augenstein and C. Rockstuhl, "Inverse design of nanophotonic devices with structural integrity," ACS Photonics **7**(8), 2190–2196 (2020).
42. F. Wang, B. S. Lazarov, and O. Sigmund, "On projection methods, convergence and robust formulations in topology optimization," Struct. Multidisc. Optim. **43**(6), 767–784 (2011).
43. G. Zhang, D.-X. Xu, Y. Grinberg, and O. Liboiron-Ladouceur, "Topological inverse design of nanophotonic devices with energy constraint," Opt. Express **29**(8), 12681–12695 (2021).